Published in final edited form as:
Nat Photonics. 2014 June ; 8(6): 448–454. doi:10.1038/nphoton.2014.107.

Mapping distributed brain function and networks with diffuse optical tomography

Adam T. Eggebrecht[1], **Silvina L. Ferradal**[2], **Amy Robichaux-Viehoever**[3], **Mahlega S. Hassanpour**[4], **Hamid Dehghani**[5], **Abraham Z. Snyder**[1,3], **Tamara Hershey**[6], and **Joseph P. Culver**[1,2,4,*]

[1]Department of Radiology, Washington University School of Medicine, St Louis, Missouri 63110, USA

[2]Department of Biomedical Engineering, Washington University, St Louis, Missouri 63130, USA

[3]Department of Neurology, Washington University School of Medicine, St Louis, Missouri 63110, USA

[4]Department of Physics, Washington University School of Medicine, St Louis, Missouri 63130, USA

[5]School of Computer Science, University of Birmingham, Edgbaston, Birmingham B15 2TT, UK

[6]Department of Psychiatry, Washington University School of Medicine, St Louis, Missouri 63110, USA

Abstract

Mapping of human brain function has revolutionized systems neuroscience. However, traditional functional neuroimaging by positron emission tomography or functional magnetic resonance imaging cannot be used when applications require portability, or are contraindicated because of ionizing radiation (positron emission tomography) or implanted metal (functional magnetic resonance imaging). Optical neuroimaging offers a non-invasive alternative that is radiation free and compatible with implanted metal and electronic devices (for example, pacemakers). However, optical imaging technology has heretofore lacked the combination of spatial resolution and wide field of view sufficient to map distributed brain functions. Here, we present a high-density diffuse optical tomography imaging array that can map higher-order, distributed brain function. The

*Correspondence and requests for materials should be addressed to J.P.C. culverj@wustl.edu.

Author contributions

A.T.E. and J.P.C. designed the system. A.T.E. built the system. A.T.E., S.L.F., A.R.V., M.H., A.Z.S., T.H. and J.P.C. designed the experiments. A.T.E., S.L.F. and A.R.V. collected data. A.R.V. performed the Parkinson's evaluations. T.H. supervised A.R.V. A.T.E., S.L.F., M.H. and H.D. developed analysis code. A.T.E. and A.R.V. analysed the data. A.T.E., A.R.V., A.Z.S. and J.P.C. wrote the manuscript, with input from all authors.

Additional information

Supplementary information is available in the online version of the paper. Reprints and permissions information is available online at www.nature.com/reprints.

Competing financial interests

J.P.C. and Washington University have financial interests in Cephalogics LLC based on a licence of related optical imaging technology by the University to Cephalogics LLC.

system was tested by imaging four hierarchical language tasks and multiple resting-state networks including the dorsal attention and default mode networks. Finally, we imaged brain function in patients with Parkinson's disease and implanted deep brain stimulators that preclude functional magnetic resonance imaging.

Mapping distributed brain activity has transformed our understanding of brain function[1-4]. Several neurological diseases manifest as alterations in distributed brain networks, including Alzheimer's disease[5], autism spectrum disorder[6] and stroke[7]. Traditionally, brain function has been imaged with positron emission tomography (PET) and with functional magnetic resonance imaging (fMRI). However, PET uses ionizing radiation, which is not permitted as an experimental procedure in children. fMRI involves exposure to strong magnetic fields and induced electric fields and so is contraindicated in patients with implanted electronic devices (for example, deep brain stimulators, pacemakers and cochlear implants).

Optical imaging has long held promise as an alternative human brain mapping technique for situations in which either fMRI or PET is contraindicated. Optical methods utilize near-infrared spectroscopy (NIRS), a safe technique (employed in pulse oximeters) that leverages sensitivity to blood volume and oxygenation[8] to report blood-oxygen-level-dependent (BOLD) signals[9] via measurements of light absorption[10]. Traditional functional NIRS (fNIRS) imaging uses sparse arrangements of NIR photon source–detector measurements, which have significantly lower spatial resolution than fMRI[10]. Widespread use of optical neuroimaging has been limited by signal contamination from superficial tissues, poor reliability and a lack of anatomical data registration. Recent developments in high-density diffuse optical tomography (HD-DOT) have improved the outlook by providing dramatically upgraded spatial resolution[11-14] and reducing the impact of superficial tissue dynamics[15,16]. Combining these advances of HD-DOT with new approaches to register data to anatomy[17-19] could provide an opportunity to significantly improve overall image quality and reliability. Despite these advances, because of the limited field of view (FOV), HD-DOT has not yet successfully simultaneously imaged multiple distributed functional systems (for example, responses in primary visual areas together with higher-order cognitive responses such as semantic association or control of attention). Expanding the FOV of HD arrays to cover a significant portion of the head presents significant challenges in high-channel-count instrumentation, light source encoding (separating signal detected from multiple sources), fibre-optic-scalp coupling, imaging array ergonomics, data quality management and anatomical light modelling algorithms. Here, we present a diffuse optical tomography imaging system that overcomes these technical challenges through integrative advances in optical instrumentation, fibre-optic cap design, optical data registration and light modelling.

The performance of the reported HD-DOT system enables imaging distributed task-based functional responses and resting-state networks (RSNs). Mapping of multiple-order, distributed brain function was tested by replicating a landmark PET study of single-word processing[20]. Mapping of spontaneous brain activity was evaluated by mapping multiple sensory and cognitive RSNs[3] using a resting-state paradigm. Throughout both the task and rest protocols, multiple metrics of DOT image quality were evaluated against fMRI acquired

in the same subjects. To enable further comparative studies, both the HD-DOT and fMRI data have been publicly released through XNAT.org. To demonstrate optical imaging in populations in whom fMRI is precluded, we imaged functional responses and RSNs in patients with Parkinson's disease who have implanted deep brain stimulators[21]. Collectively, these studies demonstrate that advanced DOT imaging offers a practical and robust alternative to fMRI for mapping distributed brain function.

HD-DOT imaging system

In designing our HD-DOT system we focused on solving the neurophotonics challenges most crucial to imaging brain function: resolution, brain specificity, an extended FOV, anatomical specificity/co-registration of optical data, and spatial normalization for group-level analyses. We developed a 96-source and 92-detector HD-DOT system that provides more than 1,200 usable source–detector measurements (Fig. 1a,b, Supplementary Fig. 1). An adequate signal-to-noise ratio (SNR; greater than 100:1), over a dynamic range of four orders of magnitude in light level, was provided by a discrete avalanche photodiode (APD) detector channel design (Fig. 1c)[12]. Due to the tight packing, each source and detector of NIR light supports multiple measurements, thus providing significant challenges in illumination encoding and decoding. To achieve a full-field frame rate of 10 Hz (Supplementary Fig. 2) with crosstalk below 1×10^{-6} throughout the contiguous FOV, source light was encoded with a mixture of spatial (Fig. 1b), frequency (Fig. 1d) and temporal (Fig. 1e) encoding. (See Methods and Supplementary Section I for further details.)

Maintaining stable optical coupling of fibre optics to the head poses significant challenges to cap design, the objectives being optimal light coupling, efficient cap fitting (<15 min) and ergonomic comfort. The design strategy centres around a cap structure that decouples the lateral torque of the fibres (parallel to the head surface) from longitudinal flexibility (perpendicular to the head) to enable the cap to both conform to the head surface and maintain good optic–scalp coupling (Supplementary Fig. 3). To achieve this, the fibre bundles (N = 188) are suspended above the subject's chair and organized into a 'double-halo' configuration to manage fibre organization and to provide distributed support of the fibre weight around the head. The fibres are held in a suspended plastic cap with press-fit foam fittings. The plastic cap is composed of anatomically shaped panels of flexible heat-formed lightweight plastic with an inner layer of foam for comfort and stability. The fibre tips extend through the interior of the cap ~3 mm (self-adjusting length 1–4 mm), to comb through the hair and couple directly to the scalp. The resulting comfort level enabled imaging sessions that lasted for over two hours without reported discomfort. This cap design provided strong (Fig. 1f) and stable (Fig. 1g) fibre–scalp optical coupling: the mean light levels of the source–detector-pair (SD-pair) measurements decay with a characteristic log-linear fall-off over distance (Fig. 1f). The large number of SD pairs creates significant challenges in visualizing, optimizing and monitoring data quality. Therefore, real-time data integrity displays were developed to monitor coupling efficiency (Fig. 1f,h) and noise levels (Fig. 1i) during cap fitting (see Supplementary Section II for details).

To complement the hardware advancements, finite-element light-modelling[22] algorithms were developed to model the sensitivity of the full SD-pair measurement set on the subject's

head (Fig. 2a) and register the DOT data to a standard atlas space (a universal practice in PET and fMRI neuroimaging[23], Supplementary Fig. 4). Although an individual SD-pair samples both brain tissue and scalp (Supplementary Fig. 5), incorporating the >1,200 simultaneous SD pairs (at each wavelength) allows this system to retain sensitivity up to 10 mm below the pial surface and to discriminate between signals originating from the brain versus overlying tissues[16]. Variation in head size and shape causes variance in the FOV across subjects, so the group-level results include only voxels sampled in all subjects (red in Fig. 2b).

Visual responses

Visual stimuli were used to evaluate fundamental SNR and cross-modality correspondence (Supplementary Figs 6, 7 and Table 1). To match the differing point-spread functions (PSFs) of fMRI and HD-DOT, we spatially smoothed the fMRI data with a 13 mm full-width at half-maximum (FWHM) Gaussian kernel for quantitative comparisons. To measure higher-order visual areas, upstream from primary visual areas V1 and V2 we mapped the visual cortex area MT (medial temporal region of extrastriate visual cortex). MT is specialized for motion processing and is often localized using moving stimuli in fMRI studies[2,24]. These sensory tasks show a strong correspondence between HD-DOT and fMRI.

Mapping hierarchical language areas

A central cognitive task for humans is language processing. To test the HD-DOT system for mapping multiple aspects of distributed brain function, a sequence of tasks was used to isolate responses to the sensory (auditory or visual), motor and sematic aspects of language. Subjects were instructed to either listen quietly to words presented through room speakers (HD-DOT) or through headphones (fMRI) (Fig. 3a); to quietly read each word (covert reading; Fig. 3b); to imagine themselves saying each word out loud (imagined speaking; Fig. 3c); or to covertly generate a verb associated with each word (covert verb generation; Fig. 3d). Contrasting the hierarchical tasks (for example, covert verb generation versus imagined speaking) revealed strong HD-DOT activations (Fig. 3, oxy-haemoglobin (ΔHbO) contrast; see Supplementary Fig. 8 for deoxy-haemoglobin (ΔHbR) and total-haemoglobin (ΔHbT)), including Broca's area, that were spatially congruent with the fMRI responses (overlap in Fig. 3 and Supplementary Table 1). The contrast-to-noise ratio (CNR) across subjects for HD-DOT was generally within a factor of 2 of the fMRI CNR (Fig. 3 and Supplementary Fig. 8). Furthermore, the single-subject responses obtained by HD-DOT and fMRI were qualitatively similar (Supplementary Fig. 9).

Maps of resting-state functional connectivity

Imaging RSNs provides a comprehensive and stringent test of HD-DOT against fMRI because the spatial patterns of functional connectivity (FC) are complex[3,25], widely distributed[1,2,5] and highly sensitive to the location of the seed region of interest[26]. We calculated seed-based maps of FC-HD-DOT (fcDOT) and FC-fMRI (fcMRI) by computing the correlation between the time courses of particular seed regions (5-mm-radius spheres) and the time courses of all other voxels in the imaging domain[25]. Maps of multiple key RSNs were generated using seeds defined by co-registered anatomy[3] and 10 min of resting-

state data. The fcDOT sensory (visual (Vis), auditory (Aud)) and motor (Mot) subnetworks (Fig. 4a–c) displayed robust inter-hemispheric FC with contralateral homotopic regions. Quantitative fcDOT–fcMRI comparisons were computed as the spatial correlation between the fcDOT and fcMRI maps (Vis: $r = 0.84$; Aud: $r = 0.77$; Mot: $r = 0.77$). Seeds in cognitive RSNs, specifically the dorsal attention network (DAN), fronto-parietal control network (FPC) and default mode network (DMN), revealed intra- as well as inter-hemispheric FC (Fig. 4d–f) comparable to the maps obtained with fMRI (DAN: $r = 0.73$; FPC: $r = 0.83$; DMN: $r = 0.72$). A matrix of the time-course correlations between each seed pair also showed qualitative agreement between the modalities (Fig. 4g). In particular, the strong off-diagonal entries in the matrices represent robust bilateral, inter-hemisphere homotopic FC.

To evaluate the spatial scale with which borders between networks can be established, we tested how abruptly the FC maps transition between networks[26]. Resting-state maps were generated for seeds placed along a line connecting the visual cortex and area MT, a node of the DAN[4] (Fig. 4h). Systematically moving the seed along this line generated FC maps that transitioned from visual network to DAN over a span of ~1 cm for both fcDOT and fcMRI (Fig. 4i). For both modalities, FC first appeared in an anterior node of the DAN (white circle in Fig. 4j), when the seed reached position 7.

Additionally, to show that the above-described results are representative, we compared fcMRI maps to fcDOT maps using all possible seed locations on the cortex within the mutual FOV ($N = 13{,}107$) using spatial correlation (Supplementary Fig. 10). Importantly, the agreement between modalities was strong (mean $r = 0.72$) and smooth across the surface of the cortex, demonstrating that fcDOT performs robustly across the large FOV without dropouts or position-dependent artefacts.

Maps of RSNs of subjects with implanted electrodes

Finally, to measure brain function in individuals in whom MRI is precluded, we imaged functional activations and mapped RSNs in three patients (aged 68, 74 and 76 years) with Parkinson's disease. Each Parkinson's disease patient had deep brain stimulation (DBS) electrodes bilaterally implanted in the subthalamic nucleus (Fig. 5a). Written informed consent was obtained in all cases, and experimental oversight was provided by the local Internal Review Board. The Parkinson's disease patients were scanned with the DBS active at clinically optimal settings. We used an atlas-derived head model for analysis[18,27] (see Supplementary Section III for details). Responses to hearing words (Fig. 5b) were located bilaterally over the temporal cortex, as in the healthy subjects (Fig. 3a). Additionally, FC maps (Fig. 5c–e) of the visual, motor and DAN RSNs exhibited topographies comparable to those obtained in the healthy subjects (Fig. 4a,c,d), especially homotopic functional connectivity with seeds in the visual cortex.

Public release of HD-DOT and fMRI data on XNAT

Public data have become an important resource within the MRI neuroimaging community[28]. To demonstrate the feasibility of releasing HD-DOT data and to enable further comparative

studies of subject-matched HD-DOT and fMRI data sets, the data are publically accessible through XNAT.org (Supplementary Fig. 11 and Supplementary Section IX).

Discussion

We have demonstrated several advances in HD-DOT functional neuroimaging: (1) mapping hierarchically organized responses to single word stimuli (Fig. 3), (2) mapping multiple higher-order RSNs (Fig. 4) and (3) functional neuroimaging of patients in whom MRI is precluded (Fig. 5). These advances were enabled by several integrative technical innovations: (1) high channel-count optical instrumentation, (2) large FOV fibre-optic cap, (3) full-head anatomical light modelling and (4) analysis of functional DOT data at the group level in a standard atlas space. In the subjects where fMRI was possible, HD-DOT was validated through voxel-wise comparisons to fMRI. Finally, both the HD-DOT and fMRI data sets have been publically released through XNAT.org.

The largest previously described contiguous optical imaging systems have used 24 to 36 detectors (usually with an equivalent source count)[12-14,29,30]. Optical elements were either placed in a sparse array (>3 cm spacing) covering most of the adult head[29,30], or placed in a high-density array (<1.5 cm spacing) but with a commensurately smaller FOV[12-14] (for example, imaging only one side of the motor cortex in one hemisphere[13]). Thus, the trade-off between resolution and FOV previously prevented detailed imaging of distributed brain function.

In comparing fMRI to HD-DOT we are comparing two modalities with inherently different PSFs, with HD-DOT at 13 mm and typical fMRI processing at ~6 mm. Our primary aim is to validate the HD-DOT images. We have therefore focused our comparison on data with matched PSFs, where the fMRI data are smoothed to HD-DOT resolution. However, for reference we also processed the fMRI language task data with a 6 mm smoothing kernel typical of standard fMRI processing[1,31] (Supplementary Fig. 8 and Table 2). Although some differences can be observed between the two fMRI data sets, the predominant features and loci are qualitatively similar. The spatial overlap measures between HD-DOT and fMRI are similar for two tasks (hearing words and covert reading), while moderately lower for two others (imagined speaking and covert verb generation) when using 6 mm smoothing rather than 13 mm smoothing for fMRI.

Although sparse optical systems have demonstrated initial feasibility for optical imaging of language tasks[32], the previous studies did not separate the hierarchy of areas, as has been done with the paradigms used here. The extended coverage of the HD-DOT system facilitated imaging of the distributed nature of language processing and isolation of the responses in the auditory, visual, sensorimotor and left prefrontal cortex (that is, Broca's area) (Fig. 3d).

Limited-FOV HD-DOT systems have provided proof-of-principle demonstrations that resting-state fcDOT is feasible[33], even in neonates[34]. However, these systems were capable only of demonstrating homotopic (symmetrical locus in opposite hemisphere) correlations. Resting-state studies using large FOV, sparse NIRS systems have also been reported[35,36].

However, sparse systems lack the spatial resolution necessary to adequately resolve hemodynamic signals at a gyral scale[11]. With fcMRI, where anatomy co-registration is inherent, RSN analysis is exquisitely sensitive to anatomical seed location[1,2,26]. By providing consistent SNR and resolution over an extended FOV, the HD-DOT system presented here provides access to multiple RSNs and enables the visualization of details not possible with previous DOT systems (for example, the anterior-posterior connections in the DAN and DMN networks). This HD-DOT system was able to detect narrow border regions between the discontinuous RSNs (Fig. 4h-j)[26]. Throughout, these resting-state fcDOT results demonstrate voxel-wise spatial correspondence to fcMRI (Fig. 4 and Supplementary Figs 10, 12).

HD-DOT, unlike fMRI, is limited to imaging the superficial cortex. Thus, HD-DOT cannot access deep subcortical brain structures (for example, the striatum and thalamus) or deep cortical structures (for example, the insula and operculum). This limitation is potentially a problem in mapping RSNs, as HD-DOT cannot access all nodes in some networks. However, every known RSN has nodes in the superficial cortex[1,3]. Therefore, although deep structures are out of range, a lesion within one area of the brain will often have effects that can be measured via disruptions in cortical–cortical node FC[7]. Thus, although constrained to the superficial cortex, HD-DOT can potentially monitor the resting-state dynamics in at least portions of all of the major described networks.

A recent special issue on fNIRS[37] captured a snapshot of the great advancements made during the years since the first seminal papers on fNIRS in 1993. The breadth and variety of studies in this special issue point towards many extensions to the results of this Article. Full head coverage has yet to be achieved with HD-DOT, but could be achieved with less than a 50% increase in FOV compared to the current system. Although the present cap is more comfortable than previous smaller caps because of the balanced weight management, wearability could be greatly advanced over the present system[38]. Here, we used subject-specific MRI, but in many applications subjects will probably not have an anatomical MRI and will require atlas-derived anatomy[18,27]. The image quality demonstrated here with haemoglobin contrasts could potentially be extended to other optical contrasts[39]. For example, recent fluorescence measurements in humans[40] suggest the possibility of HD-DOT using molecular imaging contrasts[41]. Similarly, recent transcranial measurements of light coherence during functional activations[42,43] point towards tomography of cerebral blood flow in humans.

As the image quality of HD-DOT improves, the attractive features of optical techniques can be further leveraged. Here, we have demonstrated HD-DOT in Parkinson’s disease patients with implanted DBS electrodes. Importantly, patients with DBS are not candidates for fMRI because of the potential for induction of electrical currents and heating in DBS electrodes, which can result in tissue injury, magnetic field-induced device migration, or disruption of the operational aspects of the devices[21,44]. HD-DOT avoids these electro/magnetic safety concerns and dramatically reduces the risk. Other MRI-incompatible electronic implants include cochlear implants and cardiac pacemakers (330,000 MRI-incompatible cardiac pacemakers are implanted in the USA annually[45]). HD-DOT also offers a more ecologically natural scanning environment. Whereas MRI scanner noise can exceed 120 dB (ref. 46),

HD-DOT is effectively silent (~10 dB). This permits the more nuanced language studies and natural social interactions potentially useful in studies of disorders such as autism. Also, the portability of HD-DOT provides bedside monitoring in critical-care environments (for example, neonatal intensive care[34]). The optical technology presented here, combined with the demonstrated image quality, point towards optical neuroimaging as a robust, powerful and practical tool.

Methods

HD-DOT imaging system and acquisition

The continuous-wave (c.w.) HD-DOT instrument illuminated the head with light-emitting diode (LED) sources at 750 nm and 850 nm (750-03AU and OPE5T85, Roithner Lasertechnik) and utilized APD (Hamamatsu C5460-01) detectors (Fig. 1c, Supplementary Fig. 1). A key feature of the discrete detector channel design was that each detector was digitized by a dedicated 24-bit analog-to-digital converter at 96 kHz (HD-192, MOTU)[12]. Sources and detectors were coupled with fibre-optic bundles (CeramOptec, 2.5-mm-diameter bundles of 50 mm fibres, 4.2 m in length) to a flexible imaging cap held on the head with hook-and-loop strapping (Supplementary Fig. 3). The fibres were supported by a ‘double-halo’ design comprising two collinear rings that evenly manage the weight of the cap above the subject. The cap comfortably coupled the 188 optical fibres onto the scalp surface by minimizing torque (parallel to the scalp surface) while providing lateral mobility (perpendicular to the scalp). This design allowed the fibres to translate relative to the head surface. Soft pressure from the fibre management and foam springs helped hold the fibres snugly against the scalp surface.

The array had 96 source and 92 detector positions placed in two interlaced rectangular arrays with first-through fourth-nearest neighbour separations as follows: 1.3, 3.0, 3.9 and 4.7 cm. The source positions were organized into six encoding regions (Fig. 1b), each with 16 source positions that were sequentially temporally encoded (Fig. 1e) in time steps of 6.25 ms. The two wavelengths at each source position were modulated at different frequencies (Fig. 1d; even regions, 750 nm at 17.9 kHz and 850 nm at 20.8 kHz; odd regions, 750 nm at 25.0 kHz and 850 nm at 31.3 kHz, all with a 50% duty cycle). With temporal, frequency and spatial encoding, the system worked with a frame rate of 10 Hz. Further details on the system infrastructure, electronics and imaging cap are available in the Supplementary Section I. The processing steps that convert SD-pair light levels into voxelated movies of relative changes in haemodynamics can be broken into five separate phases (Supplementary Fig. 4): anatomical light modelling, light-level measurement pre-processing, image reconstruction, spectroscopy and spatial normalization. These steps are described in detail in the Supplementary Sections III, IV and VII.

fMRI acquisition

MRI scans were collected on a Siemens Trio 3T scanner. Anatomical T1-weighted MPRAGE (echo time (TE) = 3.13 ms, repetition time (TR) = 2,400 ms, flip angle = 8°, 1 × 1 × 1 mm isotropic voxels) and T2-weighted (TE = 84 ms, flip angle = 120°, 1 × 1× 4 mm voxels) scans were taken at each (subsequently referred to as T1 and T2). Functional images

were collected using a series of asymmetric gradient spin-echo echo-planar (EPI) sequences (TE = 27 ms, TR = 2,000 ms, flip angle = 90°, 4 × 4 × 4 mm voxels) to measure the BOLD contrast. To match the HD-DOT PSF, fMRI data were smoothed with a 13 mm FWHM Gaussian kernel.

Subjects

Eighteen healthy adult right-handed subjects (aged 21-45 years) were recruited for this study. All subjects had to pass MRI screening to ensure their safe participation. Informed consent was obtained for all subjects. The research was approved by the Human Research Protection Office at Washington University School of Medicine. From the initial 18 subjects, different subjects dropped out of fMRI (n = 5) and HD-DOT (n = 5), leaving eight subjects for the combined fMRI/HD-DOT study (see Supplementary Section V). Each of the eight subjects was presented each stimulus paradigm. Parkinson's disease patients with implanted DBSs (N = 3, ages 68, 74 and 76 years) also participated. Images localizing the DBS electrodes were taken immediately post-operatively as part of routine clinical care (Fig. 5a). HD-DOT data were collected with the DBS active at individualized optimal settings and while the subjects were taking their regular medications. MRI was not acquired in Parkinson's disease patients.

Stimulus protocols

For the HD-DOT stimuli, subjects were seated in a quiet sound-isolation room in an adjustable chair facing a 19-inch liquid-crystal display at a 75 cm viewing distance, with two stereo speakers placed on either side of the monitor. During fMRI, visual stimuli were presented via a projector onto a screen viewed via a mirror attached to the head coil; auditory stimuli were presented via headphones. All stimuli were driven using the Psychophysics Toolbox 3 package for MATLAB using in-house custom-built scripts. All healthy subjects were presented with the following stimuli: (1) flickering checkerboards[12], (2) an MT localizer[24], (3) a language paradigm[20] and (4) a ten-minute resting-state paradigm in which the subjects were asked to visually fixate on a cross-hair and think about nothing in particular. Parkinson's patients underwent only the auditory words and resting-state protocols. See Supplementary Sections VI, VII and VIII for details on stimulus processing and data comparisons.

Supplementary Material

Refer to Web version on PubMed Central for supplementary material.

Acknowledgments

The authors thank G. Perry and M. Olevitch for help with HD-DOT instrumentation and software, F. Miezin for setting up the MRI sequences, D. Dierker for help and patience with FreeSurfer software, and T. Nolan for assistance with MRI data acquisition. The authors also thank B. White for helpful discussion of the manuscript. This work was supported in part by the National Institutes of Health (NIH, grants R01-EB009233 (J.P.C.), R01-NS078223 (J.P.C.), T32-NS007205-30 (A.R.V) and P30-NS048056 (A.Z.S.)), an Autism Speaks Postdoctoral Translational Research Fellowship 7962 (A.T.E.), a Fulbright Science and Technology PhD Award (S.L.F.) and a McDonnell Centre for Systems Neuroscience grant (A.R.V., J.P.C. and T.H.). The funding source had no involvement in the study design, collection, analysis, interpretation of the data, writing of the paper, or the decision to submit the paper for publication.

References

1. Power JD, et al. Functional network organization of the human brain. Neuron. 2011; 72:665–678. [PubMed: 22099467]
2. Yeo BT, et al. The organization of the human cerebral cortex estimated by intrinsic functional connectivity. J. Neurophysiol. 2011; 106:1125–1165. [PubMed: 21653723]
3. Zhang D, Raichle ME. Disease and the brain's dark energy. Nature Rev. Neurol. 2010; 6:15–28. [PubMed: 20057496]
4. Corbetta M, Shulman GL. Control of goal-directed and stimulus-driven attention in the brain. Nature Rev. Neurosci. 2002; 3:201–215. [PubMed: 11994752]
5. Buckner RL, et al. Cortical hubs revealed by intrinsic functional connectivity: mapping, assessment of stability, and relation to Alzheimer's disease. J. Neurosci. 2009; 29:1860–1873. [PubMed: 19211893]
6. Kennedy DP, Courchesne E. The intrinsic functional organization of the brain is altered in autism. NeuroImage. 2008; 39:1877–1885. [PubMed: 18083565]
7. Carter AR, et al. Upstream dysfunction of somatomotor functional connectivity after corticospinal damage in stroke. Neurorehabil. Neural Repair. 2012; 26:7–19. [PubMed: 21803932]
8. Jobsis FF. Noninvasive, infrared monitoring of cerebral and myocardial oxygen sufficiency and circulatory parameters. Science. 1977; 198:1264–1267. [PubMed: 929199]
9. Ogawa S, et al. Intrinsic signal changes accompanying sensory stimulation: functional brain mapping with magnetic resonance imaging. Proc. Natl Acad. Sci. USA. 1992; 89:5951–5955. [PubMed: 1631079]
10. Obrig H, Villringer A. Beyond the visible—imaging the human brain with light. J. Cerebr. Blood Flow Metab. 2003; 23:1–18.
11. White BR, Culver JP. Quantitative evaluation of high-density diffuse optical tomography: in vivo resolution and mapping performance. J. Biomed. Opt. 2010; 15:026006. [PubMed: 20459251]
12. Zeff BW, White BR, Dehghani H, Schlaggar BL, Culver JP. Retinotopic mapping of adult human visual cortex with high-density diffuse optical tomography. Proc. Natl Acad. Sci. USA. 2007; 104:12169–12174. [PubMed: 17616584]
13. Joseph DK, Huppert TJ, Franceschini MA, Boas DA. Diffuse optical tomography system to image brain activation with improved spatial resolution and validation with functional magnetic resonance imaging. Appl. Opt. 2006; 45:8142–8151. [PubMed: 17068557]
14. Koch SP, et al. High-resolution optical functional mapping of the human somatosensory cortex. Frontiers Neuroenerg. 2010; 2:1–12.
15. Saager R, Berger A. Measurement of layer-like hemodynamic trends in scalp and cortex: implications for physiological baseline suppression in functional near-infrared spectroscopy. J. Biomed. Opt. 2008; 13:034017. [PubMed: 18601562]
16. Gregg NM, White BR, Zeff BW, Berger AJ, Culver JP. Brain specificity of diffuse optical imaging: improvements from superficial signal regression and tomography. Frontiers Neuroenerg. 2010; 2:1–8.
17. Okamoto M, Dan I. Automated cortical projection of head-surface locations for transcranial functional brain mapping. NeuroImage. 2005; 26:18–28. [PubMed: 15862201]
18. Custo A, et al. Anatomical atlas-guided diffuse optical tomography of brain activation. NeuroImage. 2010; 49:561–567. [PubMed: 19643185]
19. Eggebrecht AT, et al. A quantitative spatial comparison of high-density diffuse optical tomography and fMRI cortical mapping. NeuroImage. 2012; 61:1120–1128. [PubMed: 22330315]
20. Petersen SE, Fox PT, Posner MI, Mintun M, Raichle ME. Positron emission tomographic studies of the cortical anatomy of single-word processing. Nature. 1988; 331:585–589. [PubMed: 3277066]
21. Henderson JM, et al. Permanent neurological deficit related to magnetic resonance imaging in a patient with implanted deep brain stimulation electrodes for Parkinson's disease: case report. Neurosurgery. 2005; 57:E1063. discussion E1063. [PubMed: 16284543]

22. Dehghani H, et al. Near infrared optical tomography using NIRFAST: algorithm for numerical model and image reconstruction. Commun. Numer. Methods Eng. 2008; 25:711–732. [PubMed: 20182646]
23. Fox PT, Perlmutter JS, Raichle ME. A stereotactic method of anatomical localization for positron emission tomography. J. Comput. Assist. Tomogr. 1985; 9:141–153. [PubMed: 3881487]
24. Tootell RB, et al. Visual motion aftereffect in human cortical area MT revealed by functional magnetic resonance imaging. Nature. 1995; 375:139–141. [PubMed: 7753168]
25. Fox MD, Raichle ME. Spontaneous fluctuations in brain activity observed with functional magnetic resonance imaging. Nature Rev. Neurosci. 2007; 8:700–711. [PubMed: 17704812]
26. Cohen AL, et al. Defining functional areas in individual human brains using resting functional connectivity MRI. NeuroImage. 2008; 41:45–57. [PubMed: 18367410]
27. Ferradal SL, Eggebrecht AT, Hassanpour M, Snyder AZ, Culver JP. Atlas-based head modeling and spatial normalization for high-density diffuse optical tomography: in vivo validation against fMRI. NeuroImage. 2013; 85:117–126. [PubMed: 23578579]
28. Marcus DS, Olsen TR, Ramaratnam M, Buckner RL. The extensible neuroimaging archive toolkit: an informatics platform for managing, exploring, and sharing neuroimaging data. Neuroinformatics. 2007; 5:11–34. [PubMed: 17426351]
29. Franceschini MA, Joseph DK, Huppert TJ, Diamond SG, Boas DA. Diffuse optical imaging of the whole head. J. Biomed. Opt. 2006; 11:054007. [PubMed: 17092156]
30. Sato H, et al. A NIRS-fMRI investigation of prefrontal cortex activity during a working memory task. NeuroImage. 2013; 83C:158–173. [PubMed: 23792984]
31. Shulman GL, et al. Right hemisphere dominance during spatial selective attention and target detection occurs outside the dorsal frontoparietal network. J. Neurosci. 2010; 30:3640–3651. [PubMed: 20219998]
32. Cannestra AF, Wartenburger I, Obrig H, Villringer A, Toga AW. Functional assessment of Broca's area using near infrared spectroscopy in humans. Neuroreport. 2003; 14:1961–1965. [PubMed: 14561929]
33. White BR, et al. Resting-state functional connectivity in the human brain revealed with diffuse optical tomography. NeuroImage. 2009; 47:148–156. [PubMed: 19344773]
34. Liao SM, et al. High-density diffuse optical tomography of term infant visual cortex in the nursery. J. Biomed. Opt. 2012; 17:081414. [PubMed: 23224175]
35. Sasai S, et al. A NIRS-fMRI study of resting state network. NeuroImage. 2012; 63:179–193. [PubMed: 22713670]
36. Mesquita RC, Franceschini MA, Boas DA. Resting state functional connectivity of the whole head with near-infrared spectroscopy. Biomed. Opt. Express. 2010; 1:324–336. [PubMed: 21258470]
37. Boas DA, Elwell CE, Ferrari M, Taga G. Twenty years of functional near-infrared spectroscopy: introduction for the special issue. NeuroImage. 2014; 85(1):1–5. [PubMed: 24321364]
38. Piper SK, et al. A wearable multi-channel fNIRS system for brain imaging in freely moving subjects. NeuroImage. 2013; 8:1–8.
39. Hallacoglu B, et al. Absolute measurement of cerebral optical coefficients, hemoglobin concentration and oxygen saturation in old and young adults with near-infrared spectroscopy. J. Biomed. Opt. 2012; 17:081406. [PubMed: 23224167]
40. Habermehl C, Schmitz CH, Steinbrink J. Contrast enhanced high-resolution diffuse optical tomography of the human brain using ICG. Opt. Express. 2011; 19:18636–18644. [PubMed: 21935232]
41. Ntziachristos V, Hielscher AH, Yodh AG, Chance B. Diffuse optical tomography of highly heterogeneous media. IEEE Trans. Med. Imag. 2001; 20:470–478.
42. Liebert A, et al. Bed-side assessment of cerebral perfusion in stroke patients based on optical monitoring of a dye bolus by time-resolved diffuse reflectance. NeuroImage. 2005; 24:426–435. [PubMed: 15627584]
43. Meng L, et al. Head-up tilt and hyperventilation produce similar changes in cerebral oxygenation and blood volume: an observational comparison study using frequency-domain near-infrared spectroscopy. Can. J. Anaesth. 2012; 59:357–365. [PubMed: 22234820]

44. Oluigbo CO, Rezai AR. Magnetic resonance imaging safety of deep brain stimulator devices. Handbook Clin. Neurol. 2013; 116:73–76.

45. Kalin R, Stanton MS. Current clinical issues for MRI scanning of pacemaker and defibrillator patients. Pacing Clin. Electrophysiol.: PACE. 2005; 28:326–328.

46. Price DL, De Wilde JP, Papadaki AM, Curran JS, Kitney RI. Investigation of acoustic noise on 15 MRI scanners from 0.2 T to 3 T. J. Magn. Reson. 2001; 13:288–293.

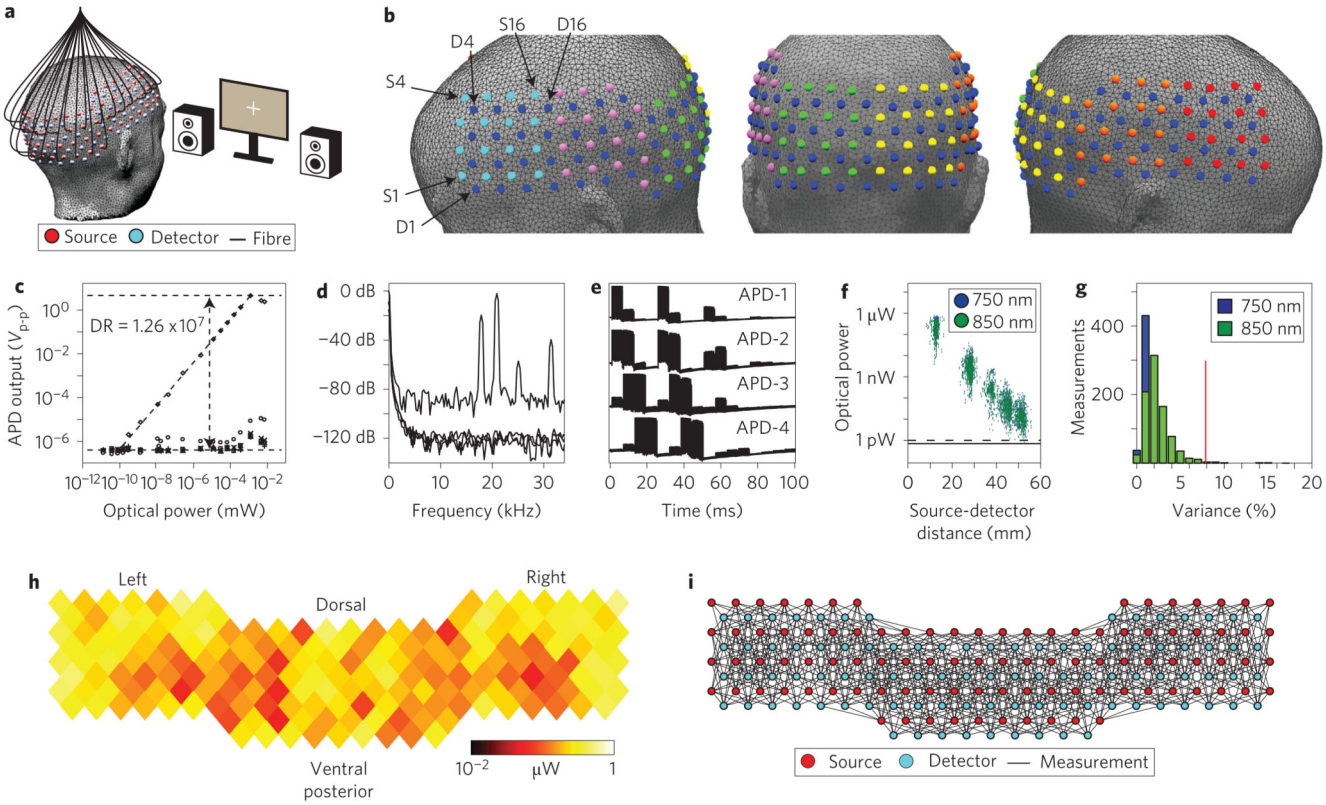

Figure 1. The HD-DOT system

a, Imaging cap structure, subject position and audiovisual stimuli for HD-DOT (subset of optical fibres shown for clarity). **b**, Interleaved square grids of detectors (blue) and sources (cyan, magenta, green, yellow, orange and red) provide a regular lattice for efficient source-detector encoding. Colours of sources represent spatially defined encoding regions (S1, D1 and so on, denote the numbering of sources/detectors). **c**, Discrete detection channels, using APDs, provide a wide dynamic range (DR) of $>10^7$ and low crosstalk of $<10^{-6}$ (diamonds, APD-1; circles, APD-2; squares, APD-3; triangles, APD-4; plus symbols, APD-5; crosses, APD-6). **d**, Each source LED is frequency encoded by region and wavelength. **e**, Time traces for four detectors demonstrate the varying light level detected throughout a single encoding frame. Within an encoding region, the source positions are temporally encoded (sequentially). **f**, The SD-pair light levels have a log-linear fall-off versus distance, characteristic of photon diffusion through biological tissue (blue, 750 nm sources; green, 850 nm sources). **g**, The temporal variance in all ~1,200 SD-pairs is used to evaluate and optimize data quality. SD-pairs with variance below 7.5% (red line) are retained for imaging. **h**,**i**, Cap fitting (~8 min) maximizes the optode coupling power across the cap (**h**) and the regional distribution of SD-pairs that pass the noise threshold (**i**, solid lines). See Methods and Supplementary Sections I and II for details.

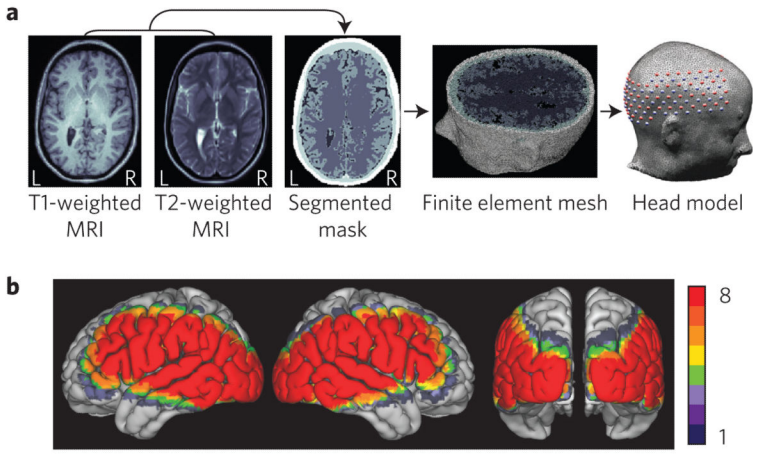

Figure 2. Finite-element modelling of NIR light propagation in a subject

a, To accurately model light propagation in a subject, the head model incorporates the head shape, internal tissue structure from the subject's anatomical MRI and optode locations. **b**, The FOV for each subject has been spatially registered and overlaid on a cortical surface view of the Montreal Neurological Institute (MNI, McGill University) atlas. Colour bar: number of subjects with sensitivity at a given location of cortex. See Methods and Supplementary Sections III and IV for details.

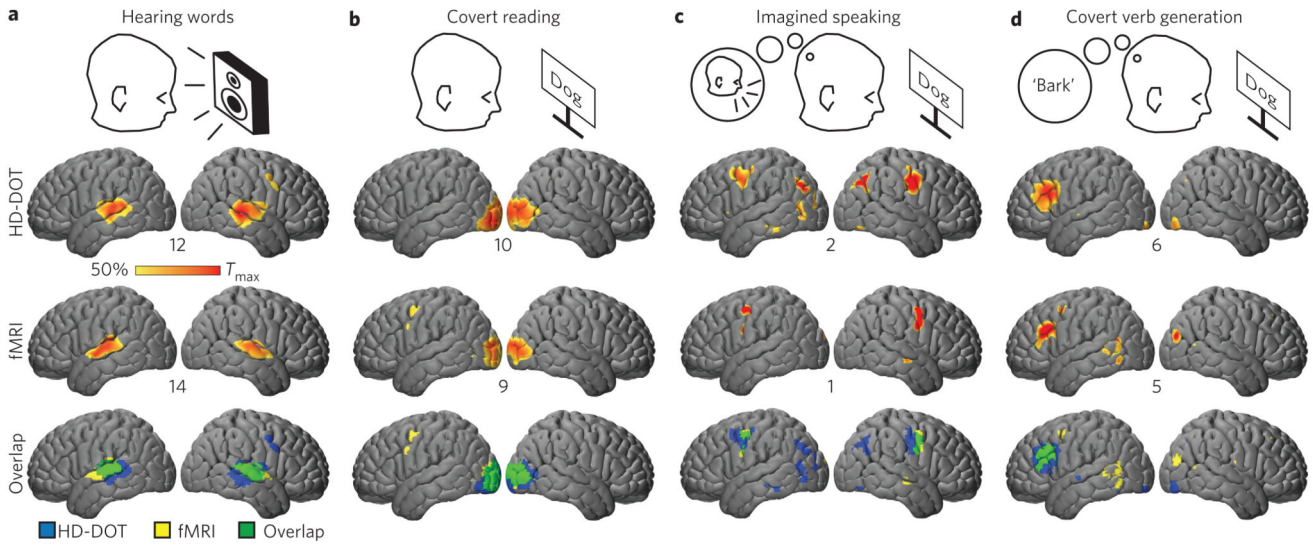

Figure 3. Evaluation of distributed brain function mapping by imaging hierarchical language processing

a-d, Differential responses throughout the FOV in response to language tasks including hearing (**a**), reading (**b**), imagined speaking (**c**) and generating words (**d**) were spatially normalized and group averaged. The HD-DOT data (ΔHbO contrast) shows excellent agreement with non-concurrently recorded fMRI (smoothed with a 13 mm FWHM Gaussian kernel) in the same subjects. The maximum *t*-value (across subjects) is displayed below each cortex (t-maps thresholded at 50% maximum). The overlap of binary masks (reflecting the 50% cutoff in the *t*-values) is displayed for each stimulus response type. See Methods and Supplementary Section IV for details.

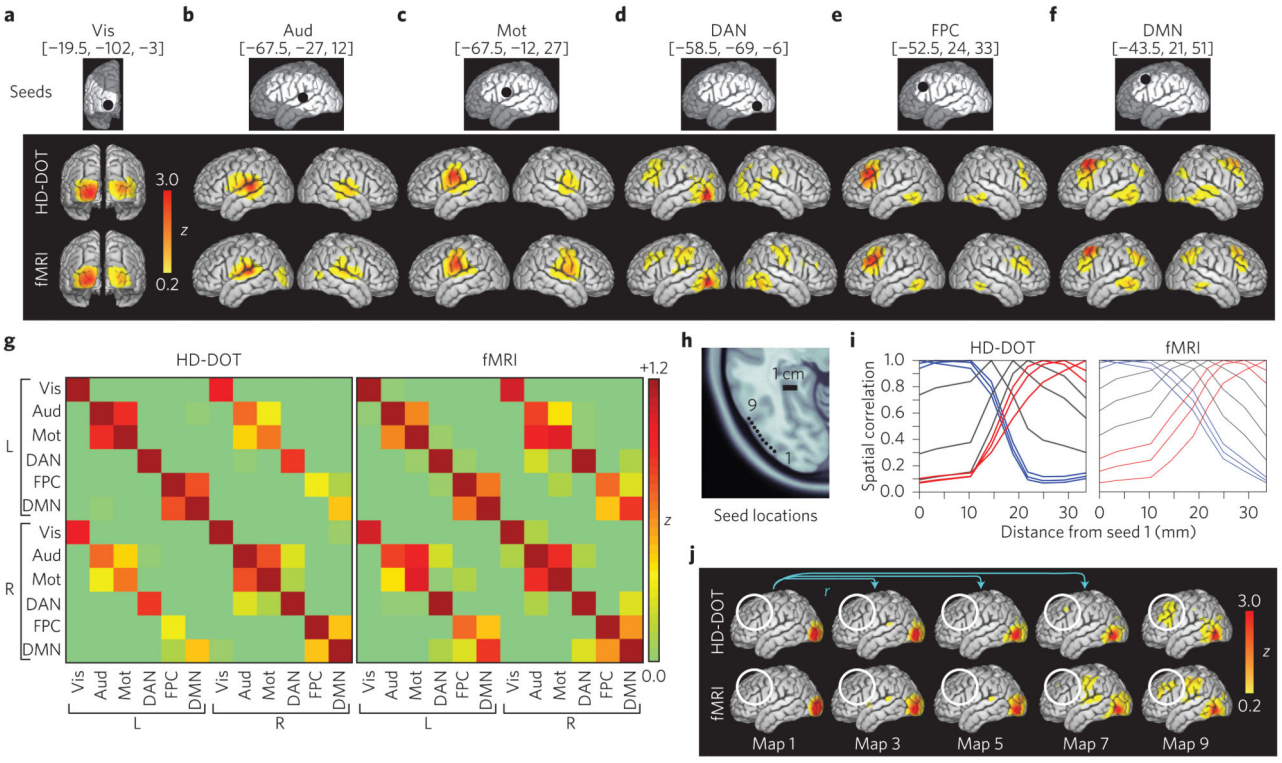

Figure 4. Mapping the functional connections of distributed brain networks

Functional connectivity maps were generated with HD-DOT (and fMRI) with seeds (black dots, MNI coordinates) representing three sensory-motor networks (visual (Vis) (**a**), auditory (Aud) (**b**), motor (Mot) (**c**)) and three higher-order networks (dorsal attention (DAN) (**d**), fronto-parietal control (FPC) (**e**) and default mode (DMN) (**f**)). **g**, Correlation matrices for the bilateral set of seeds shown in **a-f**. **h**, To explore the transition between networks, nine seeds were placed on a path connecting a seed in the occipital cortex (seed 1 in the visual network) to a seed within area MT (seed 9 in the DAN). Black scale bar, 1 cm. **i**, Strength of spatial correlation between a given seed FC map and the full set of seed FC maps. Colouring of lines reflects putative networks (blue, seeds 1-3 in the visual network; grey, seeds 4-6 within the transition zone; red, seeds 7-9 in the DAN). The spatial correlation between FC maps is strong for seeds within a network. The transition from the DAN to visual network occurs within ~1 cm. **j**, FC maps of five of the nine seeds from **h** are shown for HD-DOT and fMRI. Anterior-posterior FC characteristic of the DAN is apparent starting in seed map 7 (white circle).

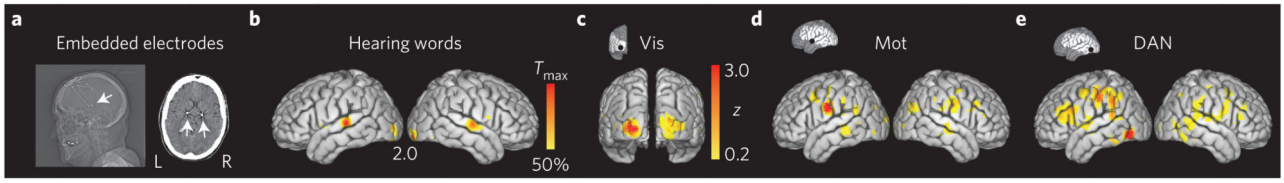

Figure 5. Measuring brain function in subjects contra-indicated for MRI

a, Imaging of Parkinson's patients with DBSs. A sagittal X-ray and an axial slice of a computed tomogram show the location of the bilaterally embedded electrodes in the subthalamic nucleus (arrows). **b**, Contrast-to-noise map of the response to hearing words measured in three patients with Parkinson's disease. The number below the cortex denotes the maximum *t*-value (ΔHbO contrast). **c-e**, Example functional connectivity maps generated at the same seeds as Fig. 4 (seed locations shown on cortex, inset).